Special Feature: Metal Forming and Processing

A New Model for Growth and Dissolution of Grain-boundary Cementite during Cyclic Vacuum Carburization

Hideaki Ikehata, Kouji Tanaka, Hiroyuki Takamiya, Hiroyuki Mizuno and Takeyuki Shimada

■**ABSTRACT**‖ In vacuum carburization of steels, a short-time carburization step is usually followed by a diffusion step to eliminate the film-like cementite (θ_{GB}) grown on the austenite (γ) grain boundary surface. In order to predict the microstructure (mainly carbon profile and the θ_{GB} amount) during this process, we investigated the boundary conditions at the carburization surface and the growth mechanism of θ_{GB} using a case hardening steel (AISI 5120). It was confirmed that the carbon content in the matrix (retained γ) at the carburization surface was around 1.4-1.6 mass%, which is consistent with $\gamma/(\gamma+\text{graphite})$ quasi-equilibrium condition. The distributions of Si and Cr in the vicinity of the γ/θ interface obtained through Field Emission Electron Probe Micro Analysis revealed that θ_{GB} grew with partitioning Cr into θ_{GB} and Si into retained γ respectively.

On the basis of these experimental results, we developed a new kinetic model for predicting microstructure during vacuum carburization. In this model, a parabolic law is assumed for the growth of θ_{GB}, and the rate-controlling process is considered to be Si diffusion rejected from θ. In contrast, the rate constant for θ_{GB} dissolution is considered to be controlled by Cr diffusion in θ. Both rate coefficients were validated through multicomponent diffusion simulation for moving velocity of the γ/θ interface. The 1-D FDM program calculated the rate of increase or decrease rate of θ_{GB} for all grid points on the basis of the local equilibrium and the diffusivity of Si or Cr which is coupled CALPHAD software. Predictions of the carbon profile and volume fraction of θ_{GB} reproduce experimental analysis results much accurately than existing models, especially for both single step carburization and the cyclic procedures involving carburization and diffusion.

■**KEYWORDS**‖ Vacuum Carburization, Metastable Equilibrium, Cementite, Growth Kinetics, Diffusion-controlled Process, Multicomponent Diffusion Simulation

1. Introduction

Vacuum carburization has been applied to commercial automotive parts as a rapid and energy-saving method for the industrial heat treatment of steel parts. The vacuum carburization allows elevated carburization temperatures, resulting in remarkably shortened operation times. Furthermore, a higher carbon content can be obtained at the surface compared to conventional gas carburization processes, due to radical reactions with decomposed species of hydrocarbon gases. On the other hand, depending on the operating conditions and geometries of the work piece, the carbon content in austenite (γ) can easily exceed the solubility limit for cementite (θ), which results in the formation of film-like γ grain boundaries. This microstructure is indicative of excess carburization, which causes embrittlement of the work piece.

The addition of Si to steels to inhibit residual θ_{GB} has been reported to be effective in preventing over-carburized microstructures;[1-3] however, this also causes poor cold and hot formability. Thus, in practice, the addition of excessive Si tends to be avoided. Instead, the chemical composition of a steel for vacuum carburization should be carefully adjusted on the basis of an understanding of the thermodynamic and kinetic effects of the alloying elements to microstructures obtained by the vacuum carburization. We focused on the effects of alloying elements with respect to two phenomena: (i) the boundary conditions during vacuum carburization, and (ii) the growth and dissolution trends of θ.

In previous work,[3-5] the dependences of both the surface carbon content and the amount of θ_{GB} on the steel composition have been interpreted on the basis of the equilibrium with graphite (Gr) derived from decomposed hydrocarbon gas. More specifically, the surface carbon content can be

determined by thermodynamic calculation in the case of steels consisting of γ and θ in equilibrium with Gr (three-phase equilibrium). For example, in the case of AISI 5120 steel (SCr420 in JIS), this is approximately 4.2 mass% at 1223 K, and the solute carbon in γ is around 1.3 mass%. Thus, it is possible to predict the carbon profile by employing a diffusion equation with a three-phase equilibrium boundary condition at the carburization surface and the equilibrium fraction of θ (hereafter, this method will be referred to as "the conventional model").

Engström[6] implemented an analogous methodology in the framework of a multicomponent diffusion solver and successfully predicted the distribution of two types of carbides precipitating in the bond of dissimilar steels. However, the conventional model has not been successfully applied to comparatively verify the amount of θ_{GB} formed during short-time carburization. Ando and Krauss[7,8] reported that the θ fraction for 1.5Cr-1.0C (mass%) steels aged at temperatures below A_{cm} increased initially, but became saturated at around 1/4 to 1/3 of the equilibrium fraction. They concluded that the retardation in the later stage was due to the slow diffusion of Cr and Si through the γ/θ ledge interface. These results suggest that a kinetic model for the growth and dissolution of θ is required. We also need to consider the complexity of the actual vacuum carburization process: the carbon profile is affected the progress of both the carburization and diffusion processes, i.e., the rate of carbon increase/decrease is not unidirectional. Thus, not only the carbon profiles but also the effects of alloying elements on θ_{GB} growth and dissolution kinetics must be modeled to obtain the evolution of the microstructure during vacuum carburization.

In this study, we developed a calculation model to predict the carbon profile and distribution of θ_{GB} during vacuum carburization consisting of cyclic carburization and diffusion processes, on the basis of the results of the following investigations:
(1) To determine the effect of the alloying elements, the macroscopic carbon profile and the carbon content in the matrix (γ phase) during vacuum carburization were analyzed using a conventional case hardening steel.
(2) The θ_{GB} distributions were quantified in order to investigate the growth behavior of grain-boundary θ. The microscopic elemental distributions in the vicinity of the γ/θ_{GB} interface were also analyzed by Field Emission Electron Probe Micro Analysis (FE-EPMA) to find out the partitioning tendencies of the alloying elements into the γ and θ phases.
(3) The theoretical growth and dissolution rates of θ were calculated for constant carbon activities under the assumption that growth and dissolution were each controlled by the diffusion of a single element. A kinetic model was developed by verifying the calculated rates with the results of a multi-component diffusion simulation and choosing an appropriate diffusional element to control the growth and dissolution rates of θ.

The diffusion equation can predict the change in local carbon solute only, and thus a discrete procedure is required to calculate the increase/decrease in θ_{GB} by estimating the instantaneous growth or dissolution rate of θ_{GB} from the local carbon activity.

A new calculation model was developed by incorporating the kinetics model described in (3) into the framework of the finite difference method (FDM). This new model was able to predict both the carbon profiles and the volume fractions of θ_{GB}. The accuracy of the model was validated by using the experimental results obtained through (1). Finally, the accuracy of the present method was confirmed experimentally by using a commercial case hardening steel and an actual vacuum carburization process, i.e., a cyclic carburization and diffusion process.

2. Experimental Investigation with a Conventional Case Hardening Steel

2. 1 Experimental Procedure

2. 1. 1 Microstructure during Carburization and Diffusion

In order to investigate the effects of chemical composition of case hardening steels on carburization behavior, we applied vacuum carburization to a typical case hardening steel (identical to JIS SCr420H steel or ANSI 5120 steel). The chemical compositions are shown in **Table 1**. For comparison with the boundary condition proposed by Morita,[3,4] both the overall carbon content and the carbon content in the γ phase for the equilibrium border of $(\gamma + \theta)/(\gamma + \theta + Gr)$ at 1223 K were also calculated by Thermo-Calc (see Table 1). **Figure 1** shows an Fe-C-Cr phase diagram, where the meaning of the two carbon contents can

Table 1 Chemical compositions of the steels used and the equilibrium carbon content (in mass%).

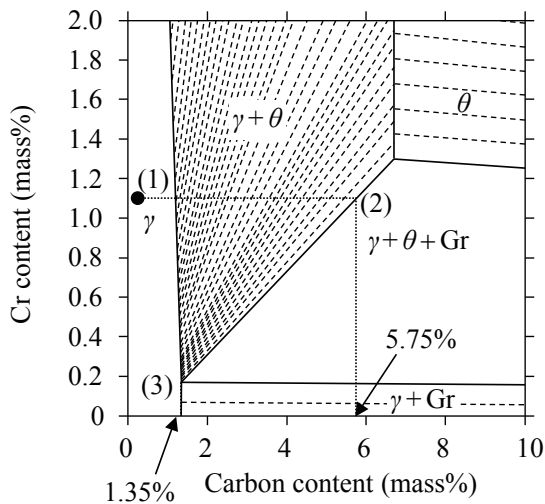| Cr	Mn	Si	C	Equilibrium border for $(\gamma + \theta)/(\gamma + \theta + Gr)$	
				Overall carbon	Carbon in γ phase (γ corner)
1.1	0.8	0.25	0.2	4.18	1.30

Fig. 1 The Fe-Cr-C phase diagram calculated by Thermo-Calc. Note that dashed lines are tie lines. The points of (1), (2) and (3) show the initial composition (Fe-1.1 mass%Cr-0.2 mass%C), the intersectional point to the equilibrium border of $(\gamma + \theta)/(\gamma + \theta + Gr)$ for Fe-1.1mass%Cr-C and the equilibrium chemical composition of the γ phase corresponding to the chemical composition of (2) respectively.

be explained as follows. When a steel having an initial composition of Fe-1.1Cr-0.2C (in mass%) ((1) in Fig. 1) is carburized, the carbon in the matrix increases to the $(\gamma + \theta)/(\gamma + \theta + Gr)$ border of the steel, labeled (2) in Fig. 1. The carbon content at (2) is around 5.75 mass%, which is the overall carbon content in Table 1, and the carbon content of the γ phase in Table 1 is 1.35 mass%, labeled (3) in Fig. 1.

The carburization process was conducted at 1223 K for 60, 240, and 1800 s. Acetylene was used as the carburization gas, and the specimens were immediately quenched in an oil bath after carburization. Prior to carburization, the specimens were homogenized for 1800 s at 1223 K. In order to determine the carbon profile and θ_{GB} behavior, a diffusion process was conducted for 300 and 1200 s after 1800 s of carburization at the same temperature (1223 K). The conditions are shown in **Table 2**.

Table 2 Carburization and diffusion process conditions.

	Carburizing	Diffusion
(a)	60 s	none
(b)	240 s	none
(c)	1800 s	none
(d)	1800 s	300 s
(e)	1800 s	1200 s

The specimens were polished and etched with picric acid in order to observe the microstructures under an optical microscope. The relationship between the volume fraction of θ and the depth from the carburization surface was determined by image analysis of the microstructures. The microstructural features were revealed by polishing the specimens parallel to the carburized surface and etching only the θ phase with a mixture of NaOH and picric acid. The distribution of carbon content was analyzed by EPMA. Glow Discharge Optical Emission Spectroscopy (GD-OES) analysis was conducted as well, in order to analyze the distribution of carbon and other elements in the vicinity of the surfaces.

2. 1. 2 Investigation of Supersaturated Carbon in the γ Phase

The solute carbon content of the matrix was estimated from the lattice constant of the retained γ phase of the R steel after quenching. The surface was polished slightly with colloidal silica in order to remove contamination. The lattice constant was measured by the Grazing-incidence XRD method, at an angle from 2° to 10°. The depth of the X-ray intrusion was estimated to be less than about 1 μm. Thus, the diffraction pattern of the retained γ phase near the surface was obtained. The lattice constants of the martensite, a^{α}, and of the retained γ phase, a^{γ},

were obtained from the diffraction pattern. The carbon content (C) of the retained γ phase was calculated by Eq. (1), proposed by Tomota,[9] where the calculated carbon content is the average over the X-ray intrusion area.

$$C \text{ (in mass\%)} = (a^\gamma - 0.3572 \times a^\alpha / 0.28664) / 0.0331 \tag{1}$$

A microscopic line analysis of C, Cr, and Si in the θ phase and the matrix near a θ-matrix interface was conducted by FE-EPMA, using the specimen carburized for 1800 s.

2. 2　Results

2. 2. 1　Microstructure

Figure 2 shows sectional microstructures after etching with picric acid. The dark network-like structure near the surface is θ_{GB}. It is confirmed that this structure exists already there after 60 s of carburization. As seen in Figs. 2(a)-(c), the film-like θ_{GB} became thicker and the carburized area extended deeper into the specimen as carburization progressed. Moreover, Figs. 2(d) and (e) reveal that as diffusion proceeded, the θ_{GB} became thinner and disappeared altogether in the sample's interior.

The microstructures parallel to the carburization surfaces are shown in **Fig. 3**. Only the θ phase was enhanced by etching with a mixture of NaOH and picric acid. These structures precipitated uniformly along the grain boundaries of the γ phase; they were confirmed to be the θ phase by XRD analysis, and their chemical composition was determined. **Figure 4** shows the relationship between the volume fraction of θ and depth from the carburization surface, obtained by image analysis of the microstructures in Fig. 3. The amount of θ increased with the progress of the carburization process. Conversely, the progress of the diffusion process dispersed the θ_{GB}.

The macroscopic distributions of elements obtained by EPMA line analysis are shown in **Fig. 5**. It was confirmed that the carburized layers thickened with the progress of carburization, but the surface was constantly around 1.2-1.3 mass% in all carburization processes. However, large amounts of θ were observed around the carburization surface, and the amounts varied with the carburization time as shown in Figs. 2 and 3. In particular, a fairly high carbon content was expected in the case of the specimen carburized for 1800 s.

Figure 6 shows the distributions of carbon content as obtained by GD-OES analysis. The values at depths
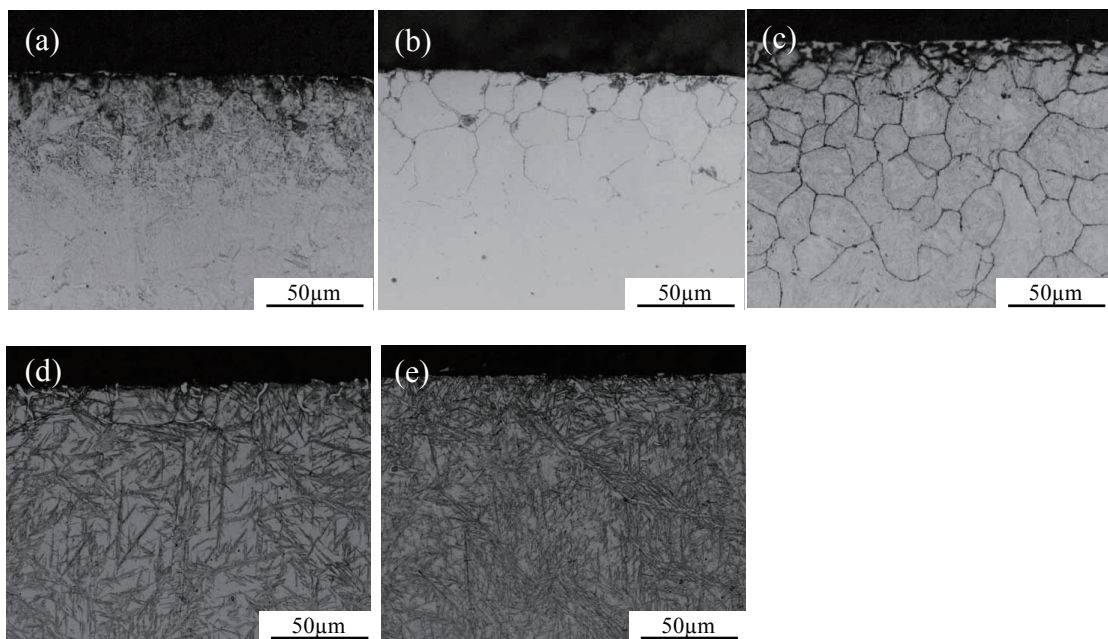

Fig. 2　Results of microstructural observations parallel to the carburizing direction after etching using picral acid. (a) Carburized for 60 s. (b) Carburized for 240 s. (c) Carburized for 1800 s. (d) Diffusion for 300 s after carburizing for 1800 s. (e) Carburized for 1200 s after carburizing for 1800 s.

of less than 2-3 μm are strongly influenced by surface contamination (graphite or soot) and should be ignored. The carbon content exceeded 4 mass% in the vicinity of the carburized surface and decreased gradually toward the interior of both specimens, showing good

agreement with the θ distributions as seen in Fig. 4. The carbon content of the specimen carburized for 1800 s was higher than that of the specimen carburized for 240 s. Although the carbon content decreased gradually with the progress of the diffusion process,
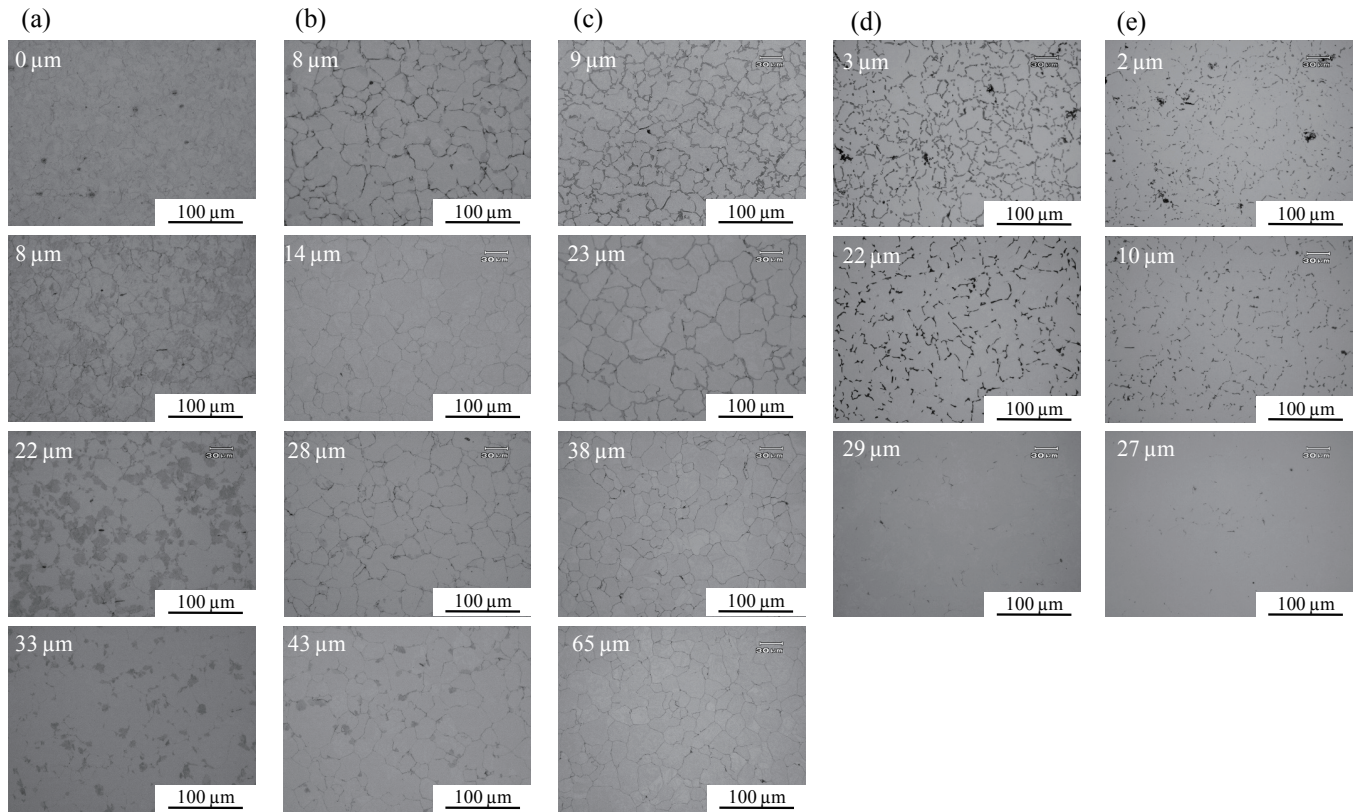
Fig. 3 Result of microstructure observations on parallel sections to the carburizing surface. All micrographs were taken after etching using NaOH and picric acid. Note that the number on left upper side of the picture represent the depth from the carburizing surface. (a) Carburized for 60 s. (b) Carburized for 240 s. (c) Carburized for 1800 s. (d) Diffusion for 300 s after 1800 s carburizing. (e) Carburized for 1200 s after 1800 s carburizing.
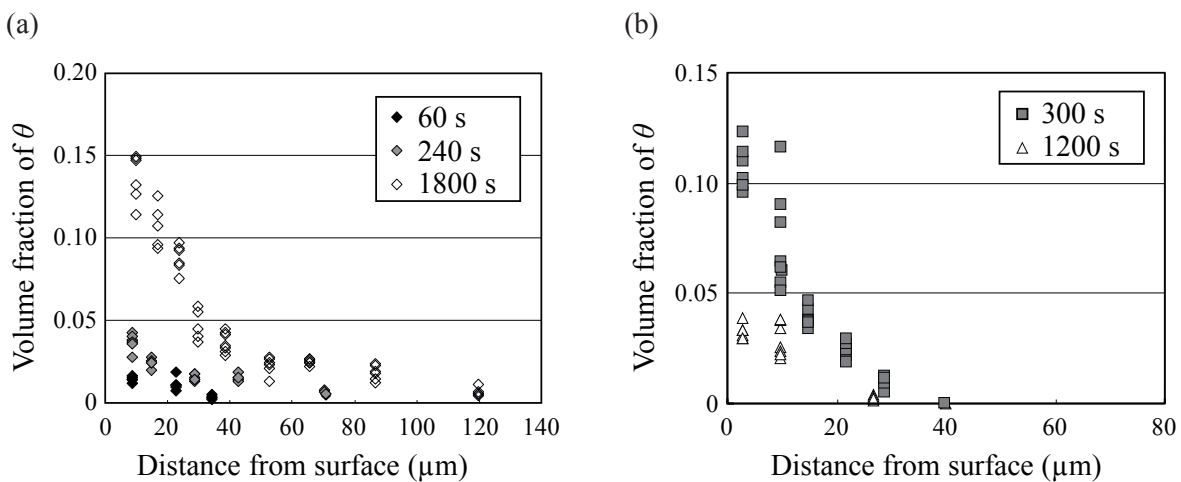

Fig. 4 Volume fractions of θ obtained from image analysis. (a) Results of carburizing processes. (b) Results of diffusion processes applied after 1800 s carburizing.

the carbon contents after 300 s of diffusion were higher than the results of EPMA analysis shown in Fig. 5. The differences between Figs. 5 and 6 were due to the fact that only the carbon content in the matrix was quantified by EPMA line analysis because the step length for EPMA line analysis was 10 μm, which is relatively large compared with the thickness of θ. Thus, the average carbon content which included carbon in θ phase was measured by GD-OES.

2. 2. 2 Equilibrium Condition at the γ/θ Interface during the Growth of θ$_{GB}$

Figure 7 shows the relationship between the depth of X-ray intrusion and the average carbon content in the γ phase. As shown in Table 1, the carbon content in the γ phase at the equilibrium border of (γ + θ)/(γ + θ + Gr) is about 1.3 mass%; however, the measured carbon content reached 1.3 mass% at 60 s and increased to around 1.4-1.6 mass% at 240 s and 1800 s. This suggests that the carbon in the γ phase becomes supersaturated with the θ phase as carburization proceeds.

Figure 8 shows the C, Si, and Cr distributions measured by FE-EPMA around θ near the carburization surface. Clearly, the amount of Si decreased and that of Cr increased inside the θ phase; however, a sharp increase in Si content and a decrease in Cr content were detected in the matrix in the vicinity of the interface. It should also be noted that the carbon
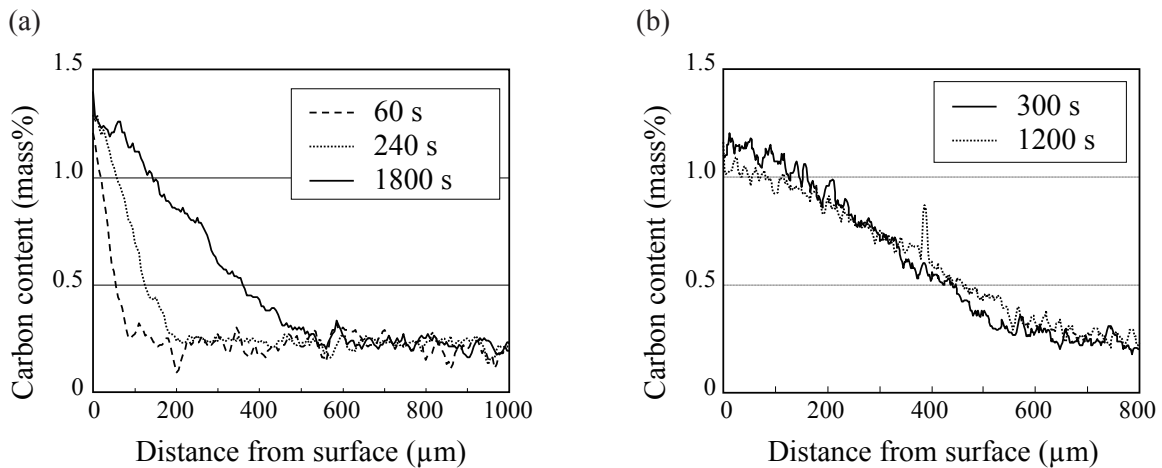
(a)   (b)

Fig. 5　Results of carbon content analysis by EPMA line analysis. (a) Results of carburizing processes. (b) Results of diffusion processes applied after 1800 s carburizing.
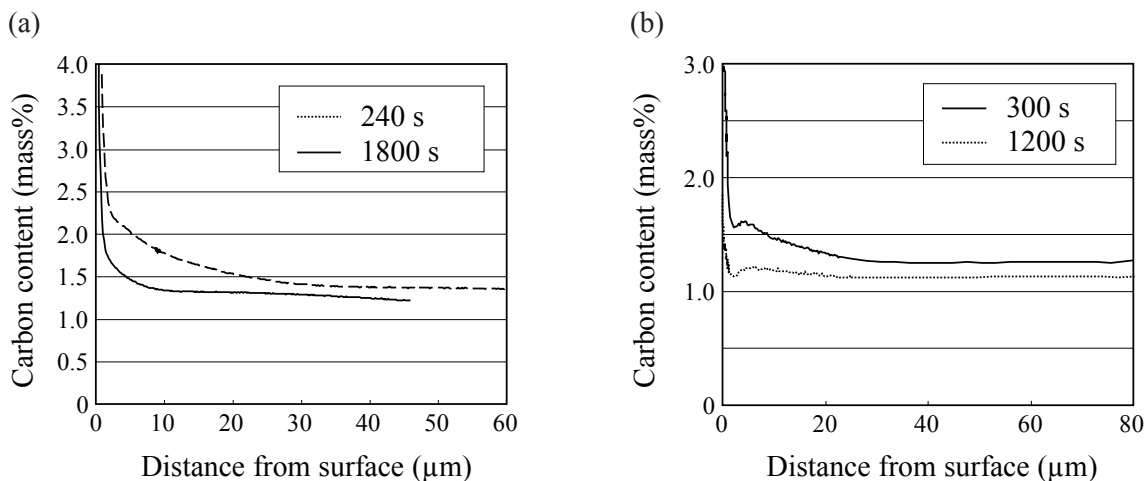
(a)   (b)

Fig. 6　Carbon content obtained by GD-OES analysis. (a) Results of carburizing processes. (b) Results of diffusion processes applied after 1800 s carburizing.

content in the matrix was around 1.6 mass%, nearly the same as the value obtained by XRD.

These experimental results lead to the following discussion. **Figure 9** shows the phase diagram of Fe-C-Cr-0.8Mn-0.25Si (mass%) at 1223 K. The thermodynamic conditions of the γ and θ phases with a supersaturated γ phase can be explained as follows, on the basis of Fig. 9. When the carbon content increases from its initial amount (1) to the ($\gamma + \theta$) two-phase area in Fig. 9 via the progress of carburization, the θ produced is less than the equilibrium amount and the carbon in the matrix becomes supersaturated with θ as mentioned above. In this case, the carbon activity at the γ/θ boundary can be assumed to be equal to that of the γ phase because of the high diffusion rate of

carbon. Additionally, the distributions of Cr and Si in γ and θ, obtained by FE-EPMA, suggest that the γ/θ interfacial condition maintains local equilibrium through partitioning of the elements.

On the basis of these results, it is assumed that the γ phase can reach the supersaturated condition indicated as (2), and its interfacial condition with respect to the θ phase is obtained by the γ phase that equilibrates the θ phase on the iso-carbon-activity line, labeled (3) in Fig. 9. The interfacial conditions of the supersaturated γ phase with the θ phase at carbon activities of 0.8 and 0.6 were labeled (3)' and (3)", respectively.

2. 2. 3 Boundary Condition of Vacuum Carburization

An estimation of the boundary condition for the vacuum carburization surface taking into consideration the supersaturated γ phase is made as follows. Because sometimes soot is produced on the carburized surfaces during vacuum carburization, the supersaturation condition with the θ phase at the surface, defined as the boundary condition, can be modeled on the assumption of thermo-dynamic equilibrium with graphite. When the growth rate of θ is low enough to
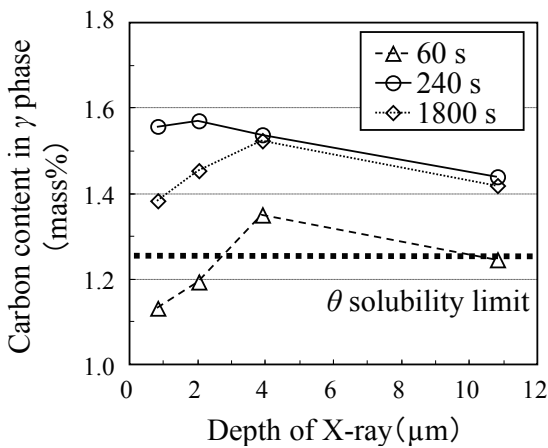

Fig. 7 Average carbon content in the γ phase of the R steel defined from the lattice constant by XRD analysis.
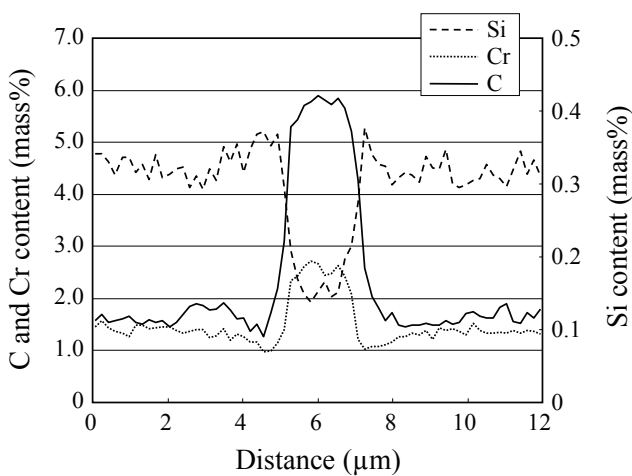

Fig. 8 Elemental distributions near θ in the R steel after 1800 s carburizing obtained by FE-EPMA.
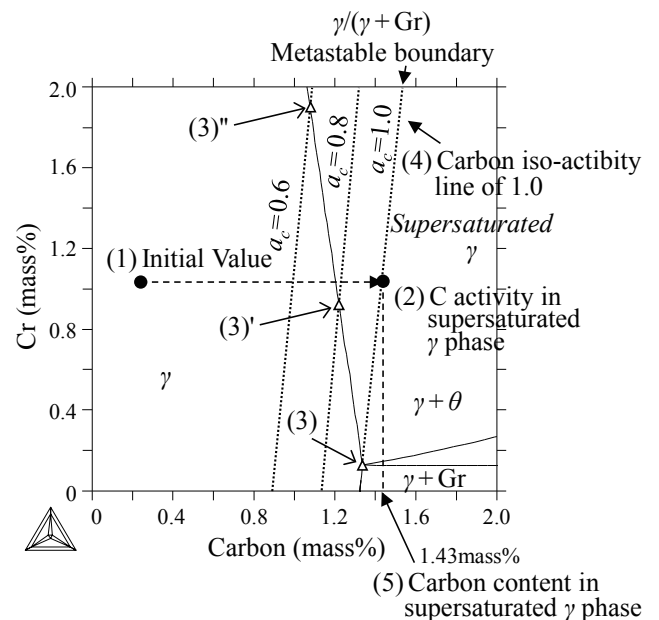

Fig. 9 The Fe-C-Cr-0.8Mn-0.25Si phase diagram at 1223 K calculated by Thermo-Calc. Note that (3), (3)' and (3)" represent the equilibrium compositions of γ phase at the γ/θ interface, when the γ phase is supersaturated with θ phase and has the carbon activity of 1.0, 0.8 and 0.6 respectively.

form supersaturated carbon in the γ phase, the carbon activity in the γ phase increases up to the $\gamma/(\gamma + \mathrm{Gr})$ metastable condition and reaches 1.0 (the referring phase is graphite) labeled (4) in Fig. 9. The carbon content in the γ phase, as calculated by Thermo-Calc, is 1.43 mass%, which shows good agreement with the values obtained by XRD and FE-EPMA. Thus, the boundary condition of vacuum carburization for a calculation model can be applied by the carbon activity under the $\gamma/(\gamma + \mathrm{Gr})$ metastable condition. This boundary condition also indicates that the local equilibrium conditions of the γ/θ interface can be obtained by the $\gamma/(\gamma + \theta)$ borders on the iso-carbon-activity line.

3. Kinetics of Grain Boundary Cementite

3.1 Calculation Method for Growth and Dissolution Rate of θ_{GB}

3. 1. 1 Equations for Diffusion-controlled Growth of θ_{GB}

In the partitioning of a single element, the thickness of the precipitate, w, can be represented by a parabolic law in terms of growth time, t : $w = \alpha\, t^{1/2}$, where α denotes a rate constant that incorporates the effect of alloying elements. This has been widely applied to the carbon diffusion-controlled growth of allotriomorphic or film-like ferrite.[10] The same equation can also be applied to the thickness of θ_{GB}, vertical to the grain boundary surface. As shown in Fig. 8, Si and Cr are partitioned into matrix and θ_{GB} during θ_{GB} growth. Therefore, Si must be rejected as a solute to allow the θ phase to grow into γ, and thus accumulates near the γ/θ interface.[11] In this respect, Si diffusion from the interface into the γ matrix could be regarded as one of the rate-controlling processes.[12] Considering the mass balance and the flux balance of Si diffusion, the parabolic growth rate constant of Si in γ, $\alpha^{\gamma}_{\mathrm{Si}}$, is theoretically calculated via Eq. (2a), which is analogous to the carbon diffusion process for the thickening of grain-boundary ferrite.[13] The terms $X^{\gamma/\theta}_{\mathrm{Si}}$ and $X^{\theta/\gamma}_{\mathrm{Si}}$ (ca. 0) denote the Si contents defined at the γ and θ sides of the interface, respectively. D^{γ}_{Si} is the diffusivity of Si in γ, and X^{0}_{Si} is the average Si content away from the γ/θ interface, or in effect, the average Si content in the steel. In general, Cr tends to be partitioned in the θ phase, and the enrichment of Cr is confirmed for the early stage of θ_{GB} precipitation. If the

thickening rate is controlled by Cr diffusion from γ to θ, then the rate constant of Cr diffusion in γ, $\alpha^{\gamma}_{\mathrm{Cr}}$, can be obtained via Eq. (2b) with equivalent symbols for the Cr contents, where D^{γ}_{Cr}, X^{0}_{Cr}, $X^{\gamma/\theta}_{\mathrm{Cr}}$, and $X^{\theta/\gamma}_{\mathrm{Cr}}$ denote the diffusivity of Cr in γ, the average Cr content, and the Cr contents defined at the γ and θ sides of the interface, respectively.

$$\alpha^{\gamma}_{\mathrm{Si}} = \frac{(X^{\gamma/\theta}_{\mathrm{Si}} - X^{0}_{\mathrm{Si}})}{\sqrt{(X^{\theta/\gamma}_{\mathrm{Si}} - X^{0}_{\mathrm{Si}})(X^{0}_{\mathrm{Si}} - X^{\gamma/\theta}_{\mathrm{Si}})}} \cdot \sqrt{D^{\gamma}_{\mathrm{Si}}} \cong \frac{X^{\gamma/\theta}_{\mathrm{Si}} - X^{0}_{\mathrm{Si}}}{\sqrt{X^{0}_{\mathrm{Si}}\, X^{\gamma/\theta}_{\mathrm{Si}}}} \cdot \sqrt{D^{\gamma}_{\mathrm{Si}}} \tag{2a}$$

$$\alpha^{\gamma}_{\mathrm{Cr}} = \frac{(X^{\gamma/\theta}_{\mathrm{Cr}} - X^{0}_{\mathrm{Cr}})}{\sqrt{(X^{\theta/\gamma}_{\mathrm{Cr}} - X^{0}_{\mathrm{Cr}})(X^{0}_{\mathrm{Cr}} - X^{\gamma/\theta}_{\mathrm{Cr}})}} \cdot \sqrt{D^{\gamma}_{\mathrm{Cr}}} \tag{2b}$$

Since Si rarely solutes in θ as described above, Si does not need be partitioned to the γ and θ phases for θ dissolution. Thus, Si diffusion is presumably not required for dissolution. In contrast, Cr, which is a strong θ former and partitions into the θ and γ phases, is expected to control the dissolution of θ_{GB}. Considering the diffusion Cr in the γ phase, the rate constant for the dissolution, $\alpha^{\gamma}_{\mathrm{Cr}}$, is given by the following equation, which is the same as Eq. (2b):

$$\alpha^{\gamma}_{\mathrm{Cr}} = \frac{(X^{\gamma/\theta}_{\mathrm{Cr}} - X^{0}_{\mathrm{Cr}})}{\sqrt{(X^{\theta/\gamma}_{\mathrm{Cr}} - X^{0}_{\mathrm{Cr}})(X^{\theta/\gamma}_{\mathrm{Cr}} - X^{\gamma/\theta}_{\mathrm{Cr}})}} \cdot \sqrt{D^{\gamma}_{\mathrm{Cr}}} \,. \tag{3a}$$

Since the Cr enrichment in θ is higher than that in γ, it is possible for the Cr diffusion in θ to be controlling the dissolution, and the rate constant, $\alpha^{\theta}_{\mathrm{Cr}}$, is obtained through Eq. (3b), in terms of the diffusivity of Cr in θ, D^{θ}_{Cr}, and the average Cr content in θ, $X^{\theta 0}_{\mathrm{Cr}}$:

$$\alpha^{\theta}_{\mathrm{Cr}} = \frac{(X^{\theta/\gamma}_{\mathrm{Cr}} - X^{\theta 0}_{\mathrm{Cr}})}{\sqrt{(X^{\gamma/\theta}_{\mathrm{Cr}} - X^{\theta 0}_{\mathrm{Cr}})(X^{\gamma/\theta}_{\mathrm{Cr}} - X^{\theta/\gamma}_{\mathrm{Cr}})}} \cdot \sqrt{D^{\theta}_{\mathrm{Cr}}} \,. \tag{3b}$$

In this study, five alloy compositions with different Si/Cr ratios were prepared on the basis of the case hardening steel grade AISI 5120 (0.21C-0.24Si-0.78Mn-1.05Cr in mass%) to investigate the thickening and thinning rates of θ_{GB}. Precipitation of θ_{GB} is likely to occur when the local carbon activity (a_C) near the grain boundaries exceeds the solubility limit of θ. On the other hand, the critical a_C for θ_{GB} dissolution depends on the volume fraction of θ_{GB} and a_C, but θ_{GB} dissolution is expected to greatly accelerate at a_C values below the solubility limit of θ. Thus, a_C values of 1.0 and 0.7 were chosen for the growth and dissolution rates, respectively. The variations in these rate constants

with a_C were investigated under the assumption of local γ/θ equilibrium. More specifically, all the parameters in Eqs. (2) and (3) were inputted via the CALPHAD thermodynamic calculation program with a constant a_C as one of the fixed state variables. The Thermo-Calc package was used in conjunction with the thermodynamic database TCFE5[14] and the mobility database MOB2.[15] The latter database provides the diffusivities for Eqs. (2) and (3). It should be noted that the diffusion coefficients were calculated after setting the chemical system as single-phase γ to consider the Cr/Si diffusion in supersaturated γ having an a_C above the θ solubility.

3. 1. 2 Calculation of θ_{GB} Growth and Dissolution by Multicomponent Diffusion Simulation

Because of experimental difficulties in controlling the arbitrarily high a_C of bulk samples of case hardening steels, a multicomponent diffusion simulation was performed to investigate the growth of θ_{GB} during which partitioning of more than two solute elements occurred. Using the DICTRA package, the one-dimensional half model shown in **Fig. 10** was set up and the velocity of the γ/θ_{GB} boundary was determined.

The five compositions described in Section 3. 1. 1 were preset for the homogeneous γ region, with differences in only Si or Cr content. The boundary condition of a_C was fixed for the left end of the model, and a θ_{GB} plate of minimal thickness was set to emerge from the right end, the assumed γ grain boundary. The overall width of the γ region was taken to be small (initially 5.0 μm) so that the θ_{GB} region was put under a nearly constant a_C due to the very high diffusivity of carbon at the calculation temperature of 1223 K. DICTRA calculates the velocity of a moving interface
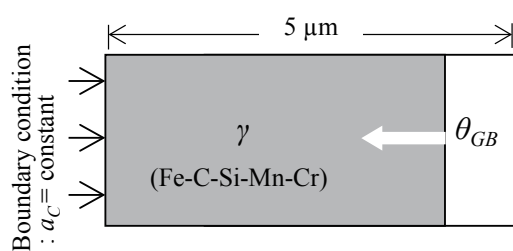

Fig. 10 One-dimensional model of film-like θ_{GB} growing from a γ grain boundary. The initial composition of the γ region is given and multicomponent diffusions are simulated both in the γ and θ_{GB} regions.

by the Newton-Rapson iteration procedure for solving under thermodynamic and kinetic limitations; i.e., local equilibrium and flux balances of all solute elements. It yielded the position of the γ/θ_{GB} interface and revealed the change in thickening or thinning rate for the range of γ compositions and boundary a_C conditions. The databases TCFE5 and MOB2 were selected to be used in DICTRA as well. Despite experimental difficulty for in situ investigation of the growth behavior of θ_{GB} during vacuum carburization, the partitioning of Cr and Si into the γ and θ_{GB} phases has been confirmed by FE-EPMA (see Fig. 8); thus, a calculation by DICTRA that incorporates partitioning of all elements into the γ and θ_{GB} phases is applicable for simulating the present experiments.

In order to investigate the growth behavior of θ_{GB}, a high carbon activity of 1.0 was applied at the left boundary in Fig. 10. For the dissolution rate of θ_{GB}, two carbon activities were applied at the left boundary. The θ_{GB} was initially grown by applying a constant carbon activity of 1.0, and then the carbon activity was lowered sufficiently to activate the dissolution of θ_{GB}. The carbon activity was set to 0.7 for the dissolution.

3. 2 Rate Control Condition for Growth and Dissolution of θ_{GB}

3. 2. 1 Calculation Results of Rate Constant Controlled by Cr or Si Diffusivity

The two growth rate constants α_{Si}^{γ} and α_{Cr}^{γ} at 1223 K were calculated; the results are plotted in **Figs. 11**(a) and (b), respectively, as a function of the carbon activity, a_C. A comparison of the Cr and Si contents of the alloys reveals that the effect of Si is much larger for both α_{Si}^{γ} and α_{Cr}^{γ}. Eqs. (2a) and (2b) suggest that the average Si content significantly affects the local equilibrium contents of Cr and Si, especially those for the γ side, $X_{Si}^{\gamma/\theta}$ and $X_{Cr}^{\gamma/\theta}$. As a_C exceeds 0.9, these rate constants increase significantly, reaching as high as 10^{-2} μm/s$^{0.5}$. The carbon activity, a_C, at the solubility of cementite is calculated to be 0.78 (with graphite as reference phase) using Thermo-Calc. Therefore, the prediction of θ_{GB} growing to a thickness of more than 1 μm in 1.8 ks as shown in Fig. 3 (average rate constant > 0.024 μm/s$^{0.5}$) is possible only by considering the high a_C of supersaturated γ.

Figures 12(a) and (b) show the rate constants α_{Cr}^{γ} and α_{Cr}^{θ} during the dissolution of θ_{GB}. The Cr content

of θ_{GB} was assumed to be the equilibrium content at an a_C of 1.0. It is confirmed that α_{Cr}^{γ} becomes positive, indicating θ_{GB} growth, when a_C is larger than the solubility limit of θ. In contrast, owing to the strong effect of the amount of Cr on α_{Cr}^{γ}, the effect of Cr on α_{Cr}^{γ} was negligible. It was also confirmed that Si had a large effect on the absolute value of the dissolution rate constants α_{Cr}^{γ} and α_{Cr}^{θ}, which decreased with increasing Si content. Figure 12(b) also shows that α_{Cr}^{θ} decreased dramatically when a_C was decreased below the solubility limit of θ.

3. 2. 2　Results of DICTRA Simulation and Comparison with Rate Constants

Figure 13 shows the simulation results of θ_{GB} growth at 1223 K with the boundary condition of $a_C = 1.0$. The thickness of the θ_{GB} region is plotted as a function of the square root of time; a linear relationship is clearly observed for all the alloys. Thus, the growth of θ_{GB} presumably follows a parabolic law, even under multicomponent solute diffusion of C, Si, Mn, and Cr. Again, the effect of the Si content (squares)
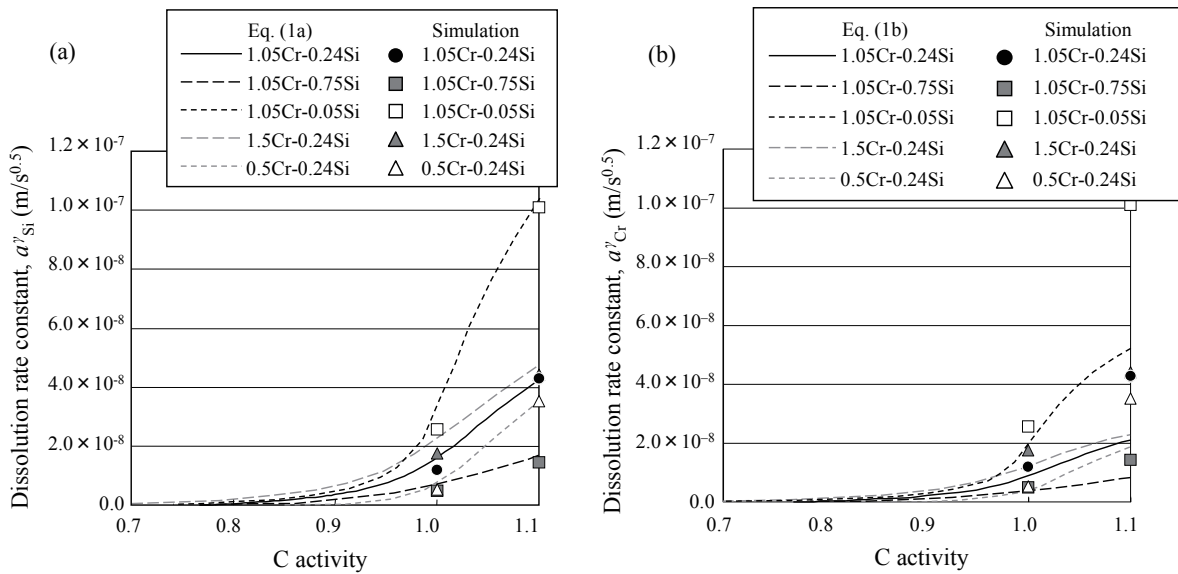

Fig. 11 Calculation of the growth rate constant of α for 5 model steels with different Si/Cr content. (a) Si-diffusion control in γ (Eq. (2a)) and (b) Cr-diffusion control in γ (Eq. (2b)). The growth rates obtained from multicomponent diffusion simulation are also shown by circle, triangle and square symbols.
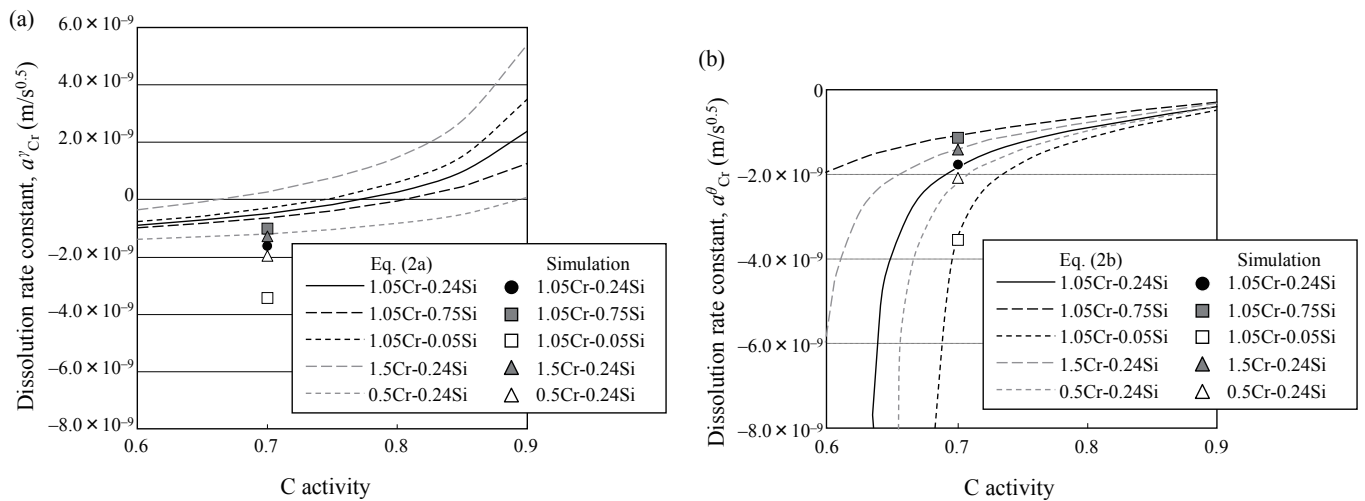

Fig. 12 Calculation of the dissolution rate constant of α for 5 model steels with different Si/Cr content. (a) Cr-diffusion control in γ (Eq. (3a)) and (b) Cr-diffusion control in θ (Eq. (3b)). The dissolution rates obtained from multicomponent diffusion simulation are also shown by circle, triangle and square symbols.

is more pronounced than that of Cr (triangles), and a decrease in Si significantly increases the growth rate of the base 1.05Cr-0.24Si alloy (AISI 5120, solid line). The experimental results for carburized steels with different Cr and Si contents[7,8] were also reproduced qualitatively.

Figure 14 shows the calculation results for dissolution behavior of θ_{GB} obtained by DICTRA. Except for the beginning and end of the dissolution, the θ_{GB} width decreases linearly with the square root of time, similarly to the growth results shown in Fig. 13. The deviation from the straight line at the beginning, which is caused by the change in the carbon distribution in the γ phase by a rapid change of the boundary condition from 1.0 to 0.7, disappears with the homogenization of the carbon profile in the matrix. At the end of the dissolution, Cr enrichment was observed, which slowed down the dissolution. In contrast, with the growth of θ_{GB}, both Cr and Si contents had a significant influence on the dissolution rate.

The rate constants of growth and dissolution were approximated linearly on the basis of the simulations and are compared in Figs. 11 and 12. In the investigated range of Cr/Si content and boundary a_C, the theoretical α_{Si}^{γ}, which is defined for the Si-diffusion-controlled process in γ and is obtainable by Eq. (2a), was demonstrated to represent the simulation results for θ_{GB} growth more accurately than α_{Cr}^{γ}. This suggests the flux of a single element, Si in this case, is dominant in

θ_{GB} growth. In the case of dissolution, α_{Cr}^{θ} reproduced the dissolution simulation results more accurately than α_{Cr}^{γ}. Thus, we conclude that the diffusivity of Cr in θ controls the dissolution of θ_{GB}, and that Eq. (3b) is suitable for the calculation of θ_{GB} dissolution.

4. Calculation Method for the θ_{GB} Fraction Distribution Induced by Vacuum Carburization

4.1 Calculation Model Based on Finite Difference Method (FDM)

4.1.1 Calculation Model for Carbon Diffusion and θ_{GB} Fraction Distribution

We developed a calculation scheme for carbon profiles and the distribution of the θ_{GB} volume fraction based on a finite difference method (FDM). As mentioned in Section 2, the surface condition of the carbon content was determined by the metastable $\gamma/(\gamma + Gr)$ equilibrium boundary between the supersaturated γ and Gr (solid circles). Though it is expected that the supersaturation of γ will decrease gradually with the evolution of θ_{GB} on the surface, the assumption of a constant surface condition is reasonable for carburization durations of a few minutes.

In the FDM, the carbon profile from the surface is calculated numerically using the difference form of the diffusion Eq. (4),
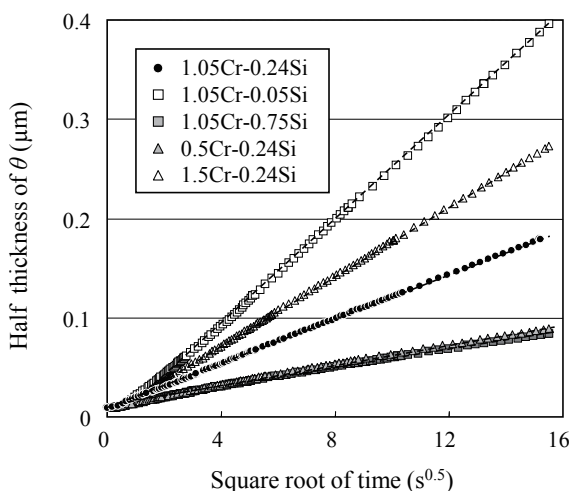

Fig. 13 Growth behavior of θ_{GB} in the 5 model steels by multicomponent diffusion simulation.
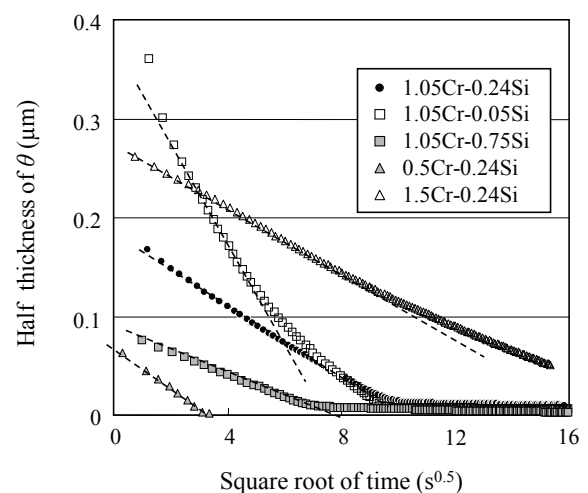

Fig. 14 Dissolution behavior of θ_{GB} in the 5 model steels by multicomponent diffusion simulation. Note that the dashed lines were applied to obtain average dissolution rate of θ.

$$X_C^\gamma(i, t_n) = X_C^\gamma(i, t_{n-1}) +$$
$$\frac{D_C^\gamma \Delta t}{\Delta z^2}\{X_C^\gamma(i-1, t_{n-1}) + X_C^\gamma(i+1, t_{n-1}) - 2X_C^\gamma(i, t_{n-1})\}, \tag{4}$$

where $X_C^\gamma(i, t_n)$ is the carbon content of the ith grid point at the nth time step of the process t_n, and D_C^γ is the diffusivity of carbon in γ, which is obtained by the MOB2 database. Δz is the distance between the $(i-1)$th and ith grids, and Δt is the time increment.

At each time step, the increment in the θ_{GB} fraction was evaluated as follows. First, $X_C^\gamma(i, t_n)$ from Eq. (4) was inputted into the thermodynamic calculation, and the resulting a_C of the supersaturated γ was taken into account when calculating the Si or Cr content at the γ/θ interface ($X_{Si}^{\gamma/\theta}$, $X_{Cr}^{\gamma/\theta}$, or $X_{Cr}^{\theta/\gamma}$ in Eqs. (2a) and (3b)). In addition to adopting the simulation model described in Section 2. 1. 2, a_C was reasonably assumed to be homogeneous in the cross-section of the γ grain at any depth, and so $X_{Si}^{\gamma/\theta}$, $X_{Cr}^{\gamma/\theta}$, and $X_{Cr}^{\theta/\gamma}$ were determined on the isoactivity lines (open triangles in Fig. 9). The rate constant $\alpha(t_n)$ was thus calculated. However, $\alpha(t_n)$ changes with time since a_C increases during carburization, and the θ_{GB} width has to be solved discretely via Eq. (5):

$$w(t_n) = \alpha(t_n)\sqrt{\tau_n + \Delta t + w_0}. \tag{5}$$

τ_n is a hypothetical duration of growth or dissolution under a constant $\alpha(t_n)$, which is expressed in Eq. (6) in terms of the thickness in the previous time step, $w(t_{n-1})$, and the hypothetical initial width, w_0.

$$\alpha(t_n)\sqrt{\tau_n} + w_0 = w(t_{n-1}) \tag{6}$$

$\alpha(t_n)$ should be chosen from Eqs. (2a) and (3b) for the growth or dissolution of θ_{GB}. w_0 should be updated to $w(t_{n-1})$ when the θ_{GB} behavior turns from growth to dissolution or vice versa. The thickness-to-volume fraction, $V_C(t_n)$, expressed in Eq. (7), was used, assuming a truncated octahedral geometry for the γ grain:

$$V_C(t_n) = w(t_n)S_V. \tag{7}$$

Here, S_V, which is the the grain boundary area per volume estimated to be $2.36/d_0$, and d_0 is the experimental average grain diameter. V_C can be converted into mole fraction, $n_C(t_n)$, with the molar volumes of γ and θ. Since a small amount of the solute carbon in γ is consumed with the growth of θ_{GB}, $X_C^\gamma(i, t_n)$ was corrected to $X_C^\gamma(i, t_n)'$ as follows, on the basis of mass conservation:

$$X_C^\gamma(i, t_n)' =$$
$$\frac{\{1 - n_C(t_{n-1})\}\,X_C^\gamma(i, t_n) - \{n_C(t_n) - n_C(t_{n-1})\}/4}{1 - n_C(t_n)}. \tag{8}$$

4. 1. 2 Conditions for Transition between Growth and Dissolution of θ_{GB}

During vacuum carburization, the gradient of carbon activity drives carbon diffusion, and the increase or decrease in carbon content does not uniformly correspond to the carburization or diffusion processes. This also means that the transition between the growth and dissolution of θ_{GB} does not coincide with the process conditions, i.e., with the carburization or diffusion process. Thus, the criteria for this transition need to be established when considering the non-equilibrium conditions for the θ and γ phases.

θ_{GB} growth continues until the carbon content of the γ phase falls below a certain amount. As mentioned earlier, since Si does not solute in θ, Si partitioning is not required for θ_{GB} dissolution. Thus, we focus on the Cr content in θ_{GB} as the criterion for the shift from growth to dissolution. We assume that θ_{GB} growth is suppressed and dissolution starts when the Cr content in θ_{GB}, $X_{Cr}^{\theta 0}$, satisfies the following condition:

$$X_{Cr}^{\theta 0} < X_{Cr}^{\theta/\gamma}, \tag{9}$$

where $X_{Cr}^{\theta/\gamma}$ is the equilibrium Cr content in θ_{GB} at a_C. Note that the inequality sign in Eq. (9) determines the flux direction of Cr at the γ/θ boundary according to Eq. (3b). In order to use the above equations, $X_{Cr}^{\theta 0}$ must be calculated during the growth or dissolution of θ_{GB}. We estimated $X_{Cr}^{\theta 0}$ by integrating the incremental contributions, $\Delta X_{Cr}^{\theta 0}$, by using the equation

$$\Delta X_{Cr}^{\theta 0} = X_{Cr}^{\theta 0}\frac{X_{Cr}^{\theta/\gamma} \times S_V \times \Delta w}{V_C(t)}, \tag{10}$$

where Δw is the incremental change in θ_{GB} width. Thermodynamic calculation predicts an increase in $X_{Cr}^{\theta/\gamma}$ for a decrease in carbon activity, meaning $X_{Cr}^{\theta 0}$ decreases with the progress of diffusion process. On the other hand, θ_{GB} starts to grow again when both the growth rate constant is positive and the following condition is satisfied:

$$V_\theta(t) < V_\theta^{eq} , \hspace{3cm} (11)$$

where V_θ^{eq} is the equilibrium volume fraction of θ_{GB}.

4. 2 Experimental Validation Procedure

As mentioned above, AISI 5120, which is a typical case-hardening steel, was used for experimental validation in this study. To investigate the growth behavior of θ_{GB}, vacuum carburization experiments were carried out for 240 s or 1800 s at 1223 K using acetylene gas. For homogenization of the temperature and the austenite microstructure, the specimens were held in vacuum for 1.8 ks before the injection of acetylene. They were then carburized and immediately quenched in an oil bath. In order to investigate the dissolution behavior of θ_{GB} during the diffusion process, the specimens were kept for 1.8 ks at the carburization temperature (1223 K) after carburization. Then, they were quenched in an oil bath. The experimental conditions used are shown in Table 2.

Macroscopic and microscopic carbon profiles were obtained by using EPMA and GD-OES, respectively. The distributions of θ_{GB} volume fraction were also determind by image analysis. Details of the experimental conditions were described in Section 2.

To simulate the actual vacuum carburization process, cyclic experiments alternating carburization and diffusion for three cycles were conducted. AISI 5120 steel was employed in the experiment. Details of the process conditions used during carburization and diffusion are shown in **Table 3**. The calculated results for carbon profiles and θ_{GB} volume fractions were compared with experimental results obtained by EPMA and image analysis, respectively.

Table 3 Cyclic carburization and diffusion
process condition.

Carburizing	Diffusion
Step 1 : 480 s	Step 2 : 600 s
Step 3 : 300 s	Step 4 : 900 s
Step 5 : 180 s	Step 6 : 1320 s

4. 3 Results of Calculations and Experiments

Our new predictive model was constructed on the basis of control over α_{Si}^γ and α_{Cr}^θ for θ_{GB} growth and dissolution, respectively. This new model was used to predict carbon profiles and θ_{GB} distributions. We concentrated on validating the surface layer ($<100\ \mu m$), where θ_{GB} precipitation is usually pronounced.

Figures 15(a) and (b) show the experimental and calculation results for AISI 5120 carburized at 1223 K for 240 s and 1800 s, respectively. The results after diffusion for 300 s and 1200 s following carburization for 1800 s are also shown in Figs. 15(c) and (d) respectively. Figure 15 also shows calculated results obtained by the conventional model, using DICTRA with the same carburization conditions.[8] Note that the distribution profiles of θ_{GB} were obtained from Fig. 4, and the results of GD-OES analysis shown in Fig. 6 were used to determine the carbon profiles. The carbon profile predicted by the present model (thick solid line) lies lower than that predicted by the conventional model in the excessive carburization region 10-20 μm from the surface, and is in better agreement with the GD-OES results. As seen in Fig. 15(a), this is due to the smaller value for the amount of θ_{GB} calculated by the kinetic approach in the present work. Additionally, the accuracy of the θ_{GB} fraction was significantly improved from that obtained using the conventional model. Although the conventional model predicted both the carbon profile and θ_{GB} after 1800 s of carburization, its tendency to overestimate can be recognized near the carburization surface.

As for the results after diffusion processes, the developed model accurately reproduces both carbon profile and θ_{GB} fraction results. In addition, although the carbon profile lies lower than the solubility limit of θ, the dissolution of θ_{GB} has not yet been completed, as shown in Fig. 15(d). This tendency cannot be represented by the conventional model, which predicts the completion of θ_{GB} dissolution after 1200 s of diffusion. This indicates that prediction of θ_{GB} behavior requires a kinetic model, leading to the conclusion that the calculation results obtained by the present model reproduced the experimental results better than the conventional model.

Moreover, a very thin (0-0.1 μm) carbon-rich film was observed on the γ grain boundary at a depth of more than 20 μm where the volume fraction of θ_{GB} is less than 0.2%. Unfortunately, the construction

of the precipitation could not be determined but no partitioning of Cr or Si was detected in this film using a field-emission-type EPMA. Therefore, the precipitations were not considered in the present model.

The experimental carbon profiles obtained under cyclic carburization and diffusion processes are shown in **Fig. 16**. Because these results were obtained by EPMA, the calculated carbon contents were slightly higher than the experimental results in the vicinity of the carburization surface after the carburization processes (Step 1, 3, and 5), but reproduced the experimental results well in the interior of specimens. **Figure 17** shows the volume fraction of θ_{GB}. It is confirmed that θ_{GB} grew near the surface after the carburization processes (Step 1, 3, and 5). The calculation results are also plotted in Figs. 16 and 17. It is confirmed that both the carbon profile and the

volume fraction of θ_{GB} reproduce the experimental results well. Thus, we conclude that our new predictive model is applicable to the actual vacuum carburization process.

5. Conclusion

In order to develop a model to predict the carbon diffusion and growth behavior of θ for vacuum carburization, we investigated the distribution of carbon content and θ volume fraction. Additionally, we also analyzed the amount of carbon solution in the matrix and elemental distributions in the vicinity of θ. These investigations yielded the following conclusion:
(1) θ was generated at grain boundaries and grew with the progress of carburization, and dissolved during the diffusion process.
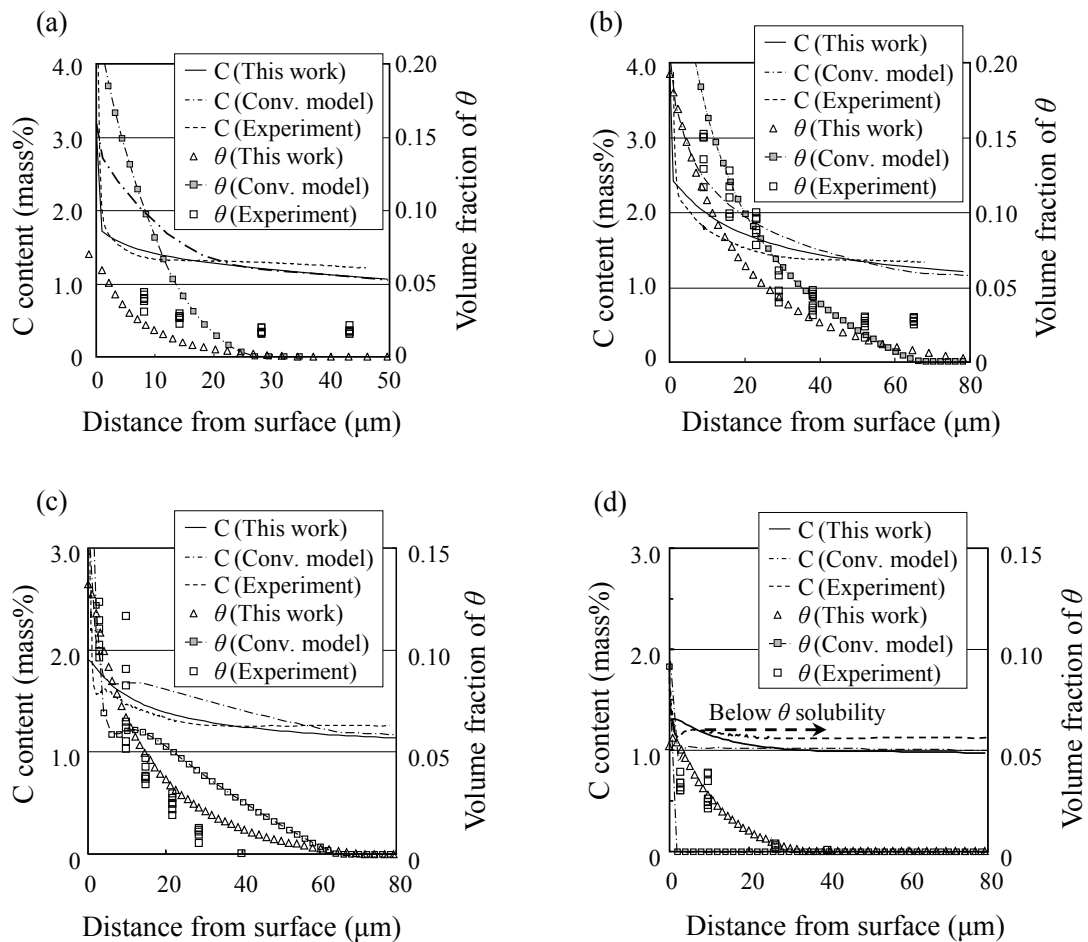(2) The carbon content in the matrix in the vicinity

Fig. 15 Calculated C concentration profiles and fraction of θ_{GB} in the vicinity of the carburized surface. These are compared with those experimentally determined results obtained by GD-OES and image analysis of the microstructure. (a) Carburization for 240 s. (b) Carburization for 1800 s. (c) Diffusion for 300 s. (d) Diffusion for 1200 s after carburization for 1800 s (about (c) and (d)).

of the carburization surface obtained by GD-OES analysis showed higher carbon content than the results obtained by EPMA.

(3) The carbon content in the matrix was 1.4-1.6 mass%, as determined by FE-EPMA and XRD. This is larger than the 1.3 mass%, which is the carbon content of the γ phase at the $(\gamma + \theta)/(\gamma + \theta + \mathrm{Gr})$ equilibrium border. This means that the matrix becomes supersaturated with carbon.
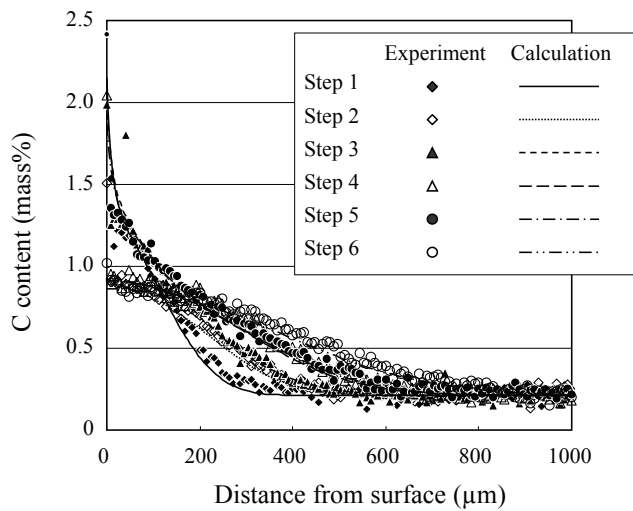

Fig. 16 Calculated and experimental C concentration profiles of AISI 5120 steel after the cyclic carburization and diffusion process as shown in Table 3.
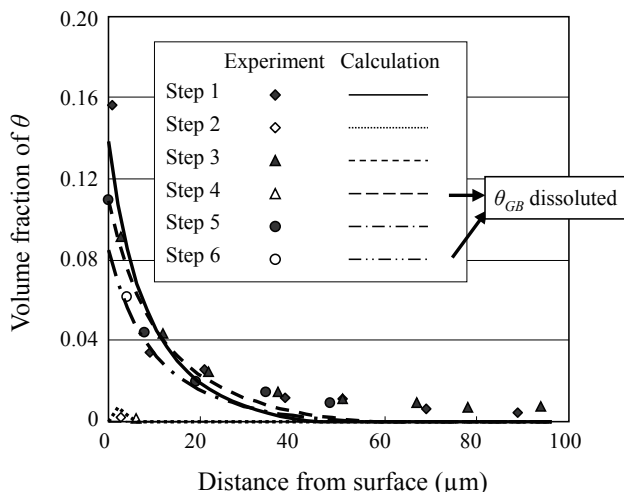
Fig. 17 Calculated and experimental fraction of θ_{GB} of AISI 5120 after the cyclic carburization and diffusion process as shown in Table 3. Note that the calculation results at Steps 4 and 6 showed the complete dissolution of θ_{GB}.

(4) The results of FE-EPMA for the vicinity of the γ/θ_{GB} interface revealed that θ grew with partitioning of Cr and Si into θ_{GB} and the matrix, respectively.

From the results described above, we developed a model to predict carbon profiles and microstructures (θ_{GB}) during vacuum carburization that can be applied to the conventional process conditions for cyclic carburization and diffusion processes. First of all, innovative kinetic calculations were performed to predict the amount of θ_{GB} obtained through rapid vacuum carburization. For every time step of inward carbon flux under the new boundary condition of supersaturated γ, the incremental change in θ_{GB} thickness was calculated on the basis of the rate-controlling model of alloy partitioning. The following conclusions were drawn from these calculations, in combination with the results of multicomponent diffusion simulation and detailed evaluation of carburized case-hardening steels.

(1) The theoretical rate constants $\alpha_{\mathrm{Si}}^{\gamma}$ and $\alpha_{\mathrm{Cr}}^{\theta}$ represented the effects of the Si and Cr steels on the growth and dissolution of θ_{GB}, respectively. Both rate constants corresponded almost exactly to the simulation results in which filmy θ_{GB} grows from or dissolves into the γ phase having different Cr and Si contents under constant carbon activities.

(2) For the excessive carburization depth range of 20 μm from the surface, the developed model reproduced reasonably well the carbon profiles detected using GD-OES. In the carburized AISI 5120 steel, significant improvements in the accuracy of the predicted θ_{GB} distributions were evident compared with the equilibrium fraction used in the conventional model.

(3) The developed model proved capable of predicting carbon profiles and θ_{GB} distributions for actual cyclic vacuum carburization consisting of alternating carburization and diffusion processes.

References

(1) Widanka, K., *Powder Metal. Progress*, Vol. 9, No. 3 (2009), pp. 165-172.
(2) Morita, T. and Matsumura, H., *CAMP-ISIJ* (in Japanese), Vol. 19 (2006), p. 1225.
(3) Morita, T. and Hanyuda, T., *Tetsu-to-Hagane* (in Japanese), Vol. 92 (2006), pp. 268-273.
(4) Morita, T., Inoue, K. and Hanyuda, T., *Electr. Furn. Steel* (in Japanese), Vol. 77, No. 1 (2006), pp. 5-9.
(5) Morita, T., *J. Jpn. Soc. Heat Treat.* (in Japanese), Vol. 49 (2009), pp. 237-242.

(6) Engström, A., Höglund, L. and Ågren, J., *Metall. Mater. Trans. A*, Vol. 25A (1994), pp. 1127-1134.
(7) Ando, T. and Krauss, G., *Acta Metall.*, Vol. 29 (1981), pp. 351-363.
(8) Ando, T. and Krauss, G., *Metall. Trans. A*, Vol. 14 (1983), pp. 1261-1269.
(9) Tomota, Y., Tokuda, H., Adachi, Y., Wakita, M., Minakawa, N., Moriai, A. and Morii, Y., *Acta Mater.*, Vol. 52 (2004), pp. 5737-5745.
(10) Liu, Z.-K., Höglund, L., Jönsson, B. and Ågre, J., *Metall. Trans. A*, Vol. 22 (1991), pp. 1745-1752.
(11) Heckel, P. W. and Paxton, H. W., *Trans. AIME*, Vol. 218 (1960), pp. 799-806.
(12) Franke, P. and Inden, G., *Proc. Symp. Nichtmetalle in Metallen '94* (1995), pp. 217-226, (DGM).
(13) Zener, C., *Trans. AIME*, Vol. 167 (1946), pp. 550-595.
(14) *TCFE5: Thermodynamic Steel Database* (2007), Thermo-Calc AB, Royal Institute of Technology.
(15) *MOB2: Mobility Database* (1998), Thermo-Calc AB, Royal Institute of Technology.

Hideaki Ikehata
  Research Fields:
    - Physical Metallurgy
    - Steels
    - Metals and Alloys
  Academic Societies:
    - The Iron and Steel Institute of Japan
    - Japan Society of Heat Treatment
    - The Japan Institute of Metals

Kouji Tanaka
  Research Fields:
    - Physical Metallurgy
    - Steels
    - Metals and Alloys
  Academic Degree: Dr.Eng.
  Academic Societies:
    - The Iron and Steel Institute of Japan
    - Japan Society of Heat Treatment
    - TMS
  Awards:
    - The Japan Institute of Metals and Materials Technical Development Award, 1996
    - R&D100 Award, 1998
    - Paper Award of Gas Turbine Society of Japan, 2002

Hiroyuki Takamiya
  Research Fields:
    - Magnetic Material
    - Physical Metallurgy
    - Titanium Alloys
  Academic Societies:
    - The Iron and Steel Institute of Japan
    - Japan Society of Heat Treatment
    - TMS
  Awards:
    - The Japan Institute of Metals and Materials Technical Development Award, 1995
    - R&D100 Award, 1996

Hiroyuki Mizuno*
  Research Field:
    - Material and Process Development of Automotive Parts
  Academic Societies:
    - The Iron and Steel Institute of Japan
    - Society of Automotive Engineers of Japan
    - Japan Society of Spring Engineers

Takeyuki Shimada*
  Research Field:
    - Process Engineering Development of Forged Products

* Aichi Steel Corporation